

Non-Hermitian-induced higher-order topological phases in acoustic fractal lattices

Shuanghuizhi Li [#], Bowei Wu [#], Tingfeng Ma ^{*}, Jiaqi Zhang, Chenbowen Lou

Zhejiang-Italy Joint Lab for Smart Materials and Advanced Structures, School of Mechanical Engineering and Mechanics, Ningbo University, Ningbo 315211, China.

[#] These authors contributed equally to this work.

^{*} Authors to whom correspondence should be addressed: matingfeng@nbu.edu.cn

Abstract

Non-Hermitian systems enable continuous and smooth tuning of topological phases through externally controllable loss/gain parameters. Without altering the intrinsic lattice structure, merely fine-tuning the intensity or spatial distribution of the loss or gain can induce the emergence of higher-order topological states, and even achieve reversible switching of topological phases. However, in non-integer dimensions, topological states induced by non-Hermiticity remain unexplored, which hinders the continuous and smooth manipulation of systems with rich higher-order topological states. By introducing a loss contrast in a fractal lattice, this study proposes a non-Hermitian route to realize higher-order topological phases in acoustic fractal lattices. Based on the tight-binding approximation, calculating the Hamiltonian of the system yields the wave-function distribution of the zero-energy modes, revealing the formation mechanisms and conditions for the topological phase transitions induced by non-Hermiticity in acoustic fractal lattices. We numerically and experimentally realize non-Hermitian-induced topological edge and corner states in a fractal structure. Furthermore, theoretical and numerical results demonstrate that merely adjusting the loss contrast can alter the degree of energy localization. This work not only establishes an effective mechanism for manipulating higher-order topology in complex fractal geometries through non-Hermiticity but also provides a theoretical framework for exploring exotic topological states of matter in non-integer dimensions.

Keywords: Non-Hermitian; Fractal geometry; Higher-order topology; Acoustics

I. Introduction

Since the proposal of the topological insulator concept, topological physics has become a research hotspot in condensed matter physics and classical wave fields. Its core advantage lies in utilizing non-trivial topological properties to achieve robust wave transport, immune to scattering from impurities and defects [1–6]. In classical wave systems, topological acoustics, as an important branch, has realized novel phenomena such as one-way sound transport and topological localization by constructing phononic crystals or acoustic metamaterials with non-trivial topological properties. This provides a completely new approach for acoustic manipulation and shows broad application prospects in areas such as acoustic filtering, directional antennas, and acoustic sensing [7–14]. With further research, the discovery of higher-order topological insulators has expanded the dimensional scope of topological physics, where the dimensionality of the topologically protected boundary states is lower than that of the bulk system, such as zero-dimensional corner states in two-dimensional systems [15–20]. The construction and manipulation of higher-order topological acoustic systems not only enrich the physical connotations of topological acoustics but also provide the possibility for achieving higher-precision acoustic localization and manipulation [21–25]. However, traditional topological acoustic research is mostly based on Hermitian systems, ignoring the inevitable energy losses in practical acoustic systems, thereby limiting its practical application value [26–28]. Due to the introduction of gain-loss mechanisms, non-Hermitian systems exhibit physical properties distinct from Hermitian systems, such as parity-time (PT) symmetry breaking, exceptional points, and the transient non-Hermitian skin effect [29–36]. In particular, non-Hermitian manipulation offers a significant advantage: without altering the original geometric structure of the system, continuous and smooth tuning of the topological phases can be achieved simply by adjusting the gain and loss parameters [37,38]. Introducing non-Hermiticity into topological acoustics forms non-Hermitian topological acoustics—such as the non-Hermitian route to higher-order topology in acoustic crystals—providing an effective approach to overcome the limitations of traditional Hermitian

topological acoustics [39].

Fractal structures, as complex geometries characterized by self-similarity and fractional dimensionality, provide a unique platform for constructing novel acoustic systems [40–42]. The multiscale nature of fractal structures allows for the manipulation of acoustic wave propagation and localization. Their combination with topological physics leads to fractal topological acoustic systems, realizing richer topological states, such as spin Chern insulators in phononic fractal lattices. However, current research on fractal topological acoustics primarily focuses on Hermitian systems. The integration of non-Hermiticity into acoustic fractal systems has not yet been fully explored, significantly hindering the dynamic and flexible tuning of higher-order states within fractal topological systems [43–45].

To systematically reveal the physical mechanisms underlying non-Hermitian-induced higher-order topological phases in acoustic fractals, this study constructs the Hamiltonian of a non-Hermitian acoustic fractal lattice based on the tight-binding approximation, clarifying the forming mechanisms and conditions for topological phase transitions in non-Hermitian fractal structures. The box-counting method is employed to quantify the fractal dimension of the energy spectrum. Combined with the analysis of the local density of states, the correlation between non-Hermitian parameters (loss intensity and distribution) and the characteristics of topological states (localization strength and frequency distribution) is established. By theoretically solving the eigenvalue equation of the Hamiltonian, the existence and distribution features of zero-energy topological corner states and edge states are obtained, providing theoretical support for subsequent numerical simulations and experimental verifications .

To verify the properties of non-Hermitian-induced acoustic fractal higher-order (e.g., quadrupole) topological insulators, we theoretically construct an acoustic fractal lattice model based on the Sierpinski carpet [46,47]. In this model, the lattice sites are equivalently replaced by acoustic resonators (such as Helmholtz resonators) with specific resonance frequencies. The equivalent hopping integrals governing the interactions between sites are realized by adjusting the dimensions of the connecting tubes between the cavities. To introduce non-Hermiticity, acoustic losses are applied at

specific lattice sites (e.g., by filling them with damping materials like acoustic sponges). This renders the equivalent on-site potentials at these locations complex, thereby breaking the Hermiticity of the system without altering its original spatial geometry. Subsequently, combining the tight-binding Hamiltonian with the theoretical solutions from the extended multiscale finite element method, full-wave numerical simulations of the eigenfrequencies and local sound pressure field distributions of acoustic waves in the non-Hermitian fractal structure are performed using the Pressure Acoustics module in COMSOL Multiphysics. Furthermore, the existence of the non-Hermitian-induced fractal higher-order topological states was verified experimentally.

II. Construction and topological phase calculation of the non-Hermitian acoustic fractal system

Figure 1 details the geometric and physical construction of the system. As shown in Fig. 1(a), the system is based on the first-generation G(1) Sierpinski carpet structure [51,52]. Although the experimental observations in this paper primarily focus on the G(1) evolution stage, its physical properties are intrinsically governed by its fractal dimension. According to the definition of the Hausdorff dimension, this fractal geometry possesses a non-integer dimension of $D \approx 1.8928$ in the iteration limit. This fractional dimension leads to hierarchical localization characteristics distinct from ordinary two-dimensional planes, providing a unique geometric platform for studying higher-order topological states.

To completely introduce the non-Hermitian-induced mechanism within the fractal framework, we refer to the conditions for generating quantized quadrupole moments in the BBH model proposed by Benalcazar, Bernevig, and Hughes [49,53], and define an extended unit cell containing 16 acoustic resonators [as shown in Fig. 1(b)]. In the traditional Hermitian BBH model, the topological phase transition relies on the strength contrast between the intra-cell coupling k_1 and inter-cell coupling k_2 ($|k_1| < |k_2|$). In our model, however, we maintain the isotropy of the spatial coupling strength, and instead induce equivalent topological behaviors through the non-uniform arrangement of non-Hermitian terms. This 16-site unit cell design exhibits significant superiority over the basic 4-site model: it not only provides sufficient spatial degrees of

freedom to precisely arrange the non-Hermitian loss contrast ($\Delta\gamma = \lambda_2 - \lambda_1$), but more importantly, it maintains a strict C_{4v} point group symmetry at the sublattice scale, which is crucial for ensuring the stability of the quadrupole states.

The solid and dashed lines within the unit cell represent alternating positive and negative acoustic couplings, respectively, which are achieved by alternately changing the connection positions of the coupling tubes. This ensures that the system possesses the π magnetic flux background in each square plaquette required to generate the quadrupole topological phase. In terms of acoustic implementation [Figs. 1(c) and 1(d)], the red rectangular blocks represent resonators introduced with additional losses, realized by opening precision holes at the top of the cavities and filling them with blue sound-absorbing materials. This design ensures that while the couplings in real space are uniform, the system meets the necessary conditions to open a topological bandgap in the complex frequency space, thereby exciting topological states protected by non-Hermiticity at the boundaries and vertices of the non-integer-dimensional fractal.

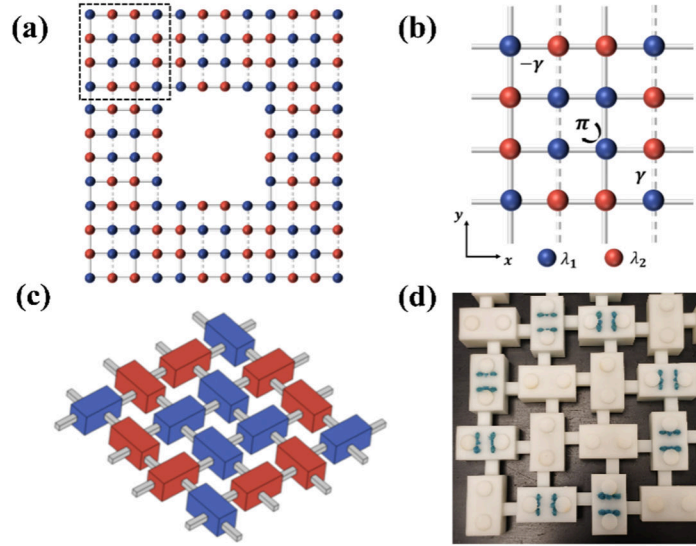


FIG. 1. Non-Hermitian-induced fractal topological insulator and its acoustic realization. (a) Schematic of the Sierpinski carpet. Solid (dashed) lines represent hoppings with a positive (negative) coupling strength. The blue (red) small spheres possess an imaginary on-site potential of λ_1 (λ_2), respectively. An enlarged view of the dashed box is shown in (b). (b) A unit-cell tight-binding model consisting of 16 lattice sites. The red (blue) lattice sites possess an imaginary on-site potential of γ . Solid (dashed) lines indicate positive (negative) couplings with a strength of γ . (c) Acoustic design of the lattice model in (b). The blue and red rectangular cuboids represent acoustic resonators with only background loss and acoustic resonators with introduced additional loss,

The effective Hamiltonian of the system can be expressed as:

$$H = \sum_i \epsilon_i c_i^\dagger c_i + \sum_{\langle i,j \rangle} t_{ij} c_i^\dagger c_j$$

Here, c_i^\dagger (c_i) represents the creation (annihilation) operator at lattice site i . To induce a quantized quadrupole moment in real space, we introduce alternating couplings with a π flux between adjacent lattice sites.

In a non-Hermitian fractal lattice, the spatial distribution of topological modes is key to identifying their physical properties. To quantitatively characterize the spatial features of the eigenstates, we define three crucial dimensionless indicators: the outer corner localization coefficient α , the inner corner localization coefficient β , and the edge localization coefficient \mathcal{E} :

(1) Outer corner localization coefficient:

This coefficient is used to quantitatively measure the concentration degree of the wave-function energy at the 0D vertices of the fractal structure ($G(1)$ outer corners). Defining $\mathcal{D}_{\text{outer corner}}$ as the set of fractal vertex lattice sites:

$$\alpha = \frac{\sum_{i \in \text{outer corner}} |\psi_{n,i}|^2}{\sum_{j=1}^N |\psi_{n,j}|^2}$$

Here, N is the total number of lattice sites in the system. When [the coefficient] approaches 1, the mode is identified as a topologically protected outer corner state, as indicated by the red branches in Fig. 2(a).

(2) Inner corner localization coefficient:

This coefficient is used to quantitatively measure the concentration degree of the wave-function energy at the 0D vertices of the fractal structure (i.e., the $G(1)$ inner corners). Defining $\mathcal{D}_{\text{inner corner}}$ as the set of fractal vertex lattice sites:

$$\beta = \frac{\sum_{i \in \text{inner corner}} |\psi_{n,i}|^2}{\sum_{j=1}^N |\psi_{n,j}|^2}$$

When β approaches 1, the mode is identified as a topologically protected inner corner state, as indicated by the green branches in Fig. 2(a).

(3) Edge localization coefficient:

This coefficient characterizes the concentration degree of the wave-function energy at the 1D edges of the fractal (excluding the vertex lattice sites). Defining $\mathcal{D}_{\text{edge}}$ as the set of all edge lattice sites:

$$\mathcal{E} = \frac{\sum_{i \in \text{edge}} |\Psi_{n,i}|^2}{\sum_{j=1}^N |\Psi_{n,j}|^2}$$

Eigenmodes with high \mathcal{E} values correspond to topological edge states distributed along the edges of the fractal skeleton, manifesting as purple branches in the complex energy spectrum.

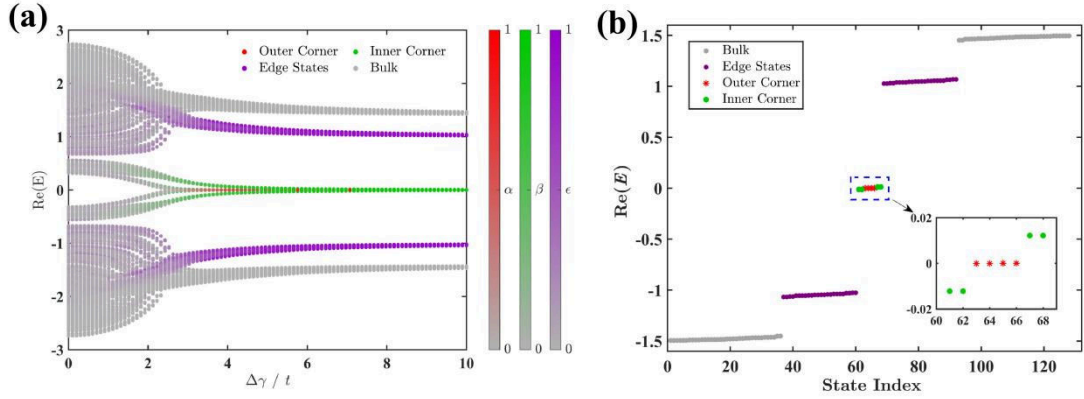


FIG. 2. Theoretical calculations of the non-Hermitian-induced fractal topological insulator. (a) The real part of the complex eigenenergies of the fractal model as a function of the loss contrast $\Delta\gamma = \lambda_2 - \lambda_1$. The red, green, and purple color scales denote the localization coefficient values for the outer corners, inner corners, and edges, respectively. (b) Energy spectrum of the fractal non-Hermitian $G(1)$ model plotted using the parameter values corresponding to an abscissa of 6 in (a).

As shown in Fig. 2(a), with the increase of the loss contrast $\Delta\gamma$, a distinct topological bandgap opens in the real-part energy spectrum. Through the color scale mappings of α , β and \mathcal{E} it can be observed that as the non-Hermitian intensity crosses the critical point, the originally degenerate bulk states split, and topological corner states with extremely high α values detach from the energy bands and become pinned near zero energy. This provides compelling evidence that the non-Hermitian loss contrast not only induces quantized quadrupole moments but also serves as the key driving force for exciting hierarchical topological states within fractal geometries.

III. Experiments and Simulations of the Non-Hermitian Acoustic Fractal Lattice

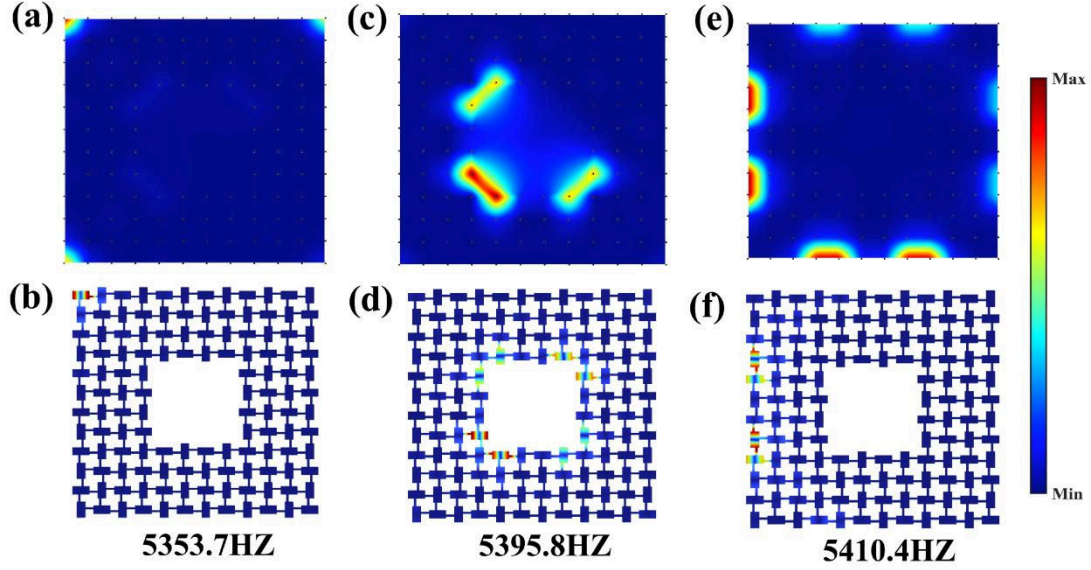


FIG. 3. Comparison between theoretical results and simulations of the non-Hermitian-induced G(1) fractal topological insulator. (a), (c), (e) Outer corner states, inner corner states, and edge states obtained from theoretical calculations, respectively. (b), (d), (f) Outer corner states, inner corner states, and edge states obtained from numerical calculations, respectively.

To visually observe the spatial evolution of the topological states, finite element analysis (FEA) is utilized to compare with the acoustic wave field distributions predicted by the tight-binding theory. Figure 3 clearly illustrates the hierarchical localization effect brought about by the non-Hermitian fractal geometry.

In the traditional BBH model, second-order topological states exist only at the four outer corners of a square lattice. However, in a fractal lattice, due to the presence of internal voids, the topological corner states exhibit fractal characteristics. Figures 3(a) and 3(c) show the theoretically predicted outer corner states and inner corner states. The outer corner states are concentrated at the outermost four vertices of the 16×16 array, whereas the inner corner states emerge at the corners of the internal cavities created by the fractal cuts.

The simulation results [Figs. 3(b), 3(d), 3(f)] perfectly reproduce this hierarchical distribution. The outer corner state exhibits extremely strong energy concentration with a very short decay length at 5353.7 Hz. The inner corner state appears at a slightly higher frequency of 5395.8 Hz. Notably, the frequencies of these corner states are strictly located within the real-part bandgap opened by the non-Hermiticity.

Furthermore, Figs. 3(e) and 3(f) display the edge state at 5410.4 Hz, with energy distributed along the outer edges of the fractal. This bandgap opened by non-Hermitian loss supports not only zero-dimensional corner states but also one-dimensional edge states, fully manifesting the hierarchical architecture of higher-order topology.

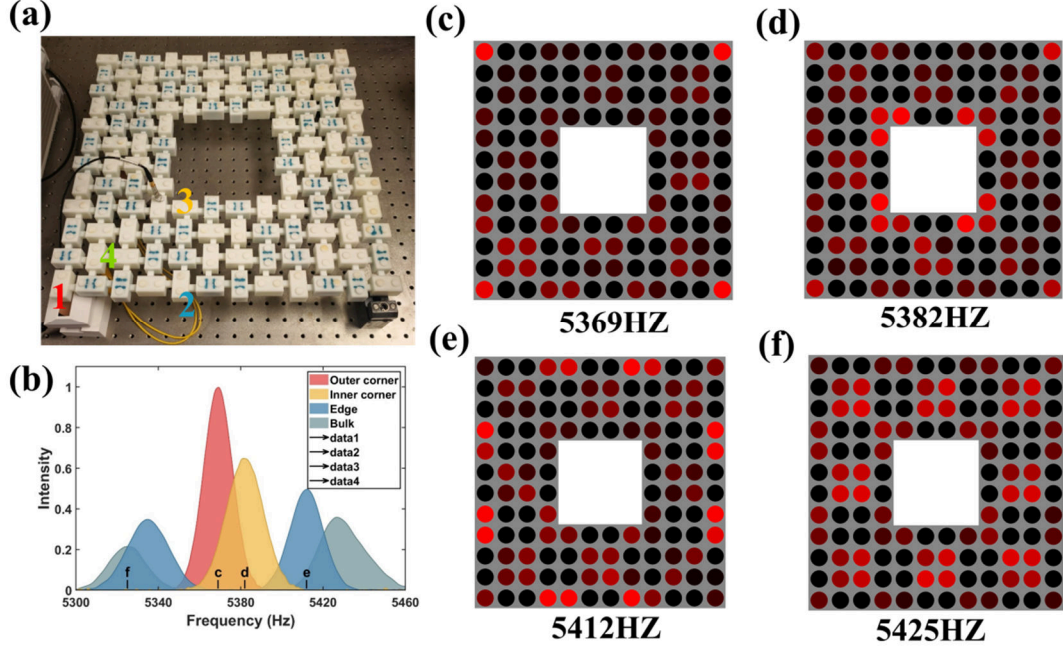


FIG. 4. Experimental observations of the HOTI in the non-Hermitian acoustic fractal lattice. (a) Photograph of the experimental sample. (b) Local density of states measured at the outer corner, edge, inner corner, and bulk sites [marked as "1", "2", "3", and "4" in (a)], indicated by red, blue, yellow, and green, respectively. (c)–(f) Experimentally measured intensity distributions at frequencies of 5369, 5382, 5412, and 5425 Hz, corresponding to the outer corner state, inner corner state, edge state, and bulk state, respectively.

To experimentally verify the existence of the non-Hermitian-induced fractal higher-order topological states, we designed and fabricated an acoustic fractal lattice composed of acoustic resonators using stereolithography 3D printing technology, and measured the acoustic response of the experimental sample with non-uniform loss. As shown in Fig. 4(a), blue sound-absorbing materials are inserted into the small holes of the rectangular resonators to introduce additional loss. Each resonator possesses two small holes that can be opened or closed by two circular cover plates. During the experiment, acoustic waves generated by a loudspeaker are introduced into the sample through the small hole on one side of the resonator, and a microphone detects the signal through the small hole on the other side of the same resonator. This measurement is

repeated for all resonators in the sample.

We select the resonator located in the middle of one edge [marked as "2" in Fig. 4(a)] and plot its response spectrum as the blue curve in Fig. 4(b). These two peaks correspond to the band-edge states. Unlike the bulk and edge state spectra, the spectra measured at the outer and inner corner resonators [marked as "1" and "3", respectively, in Fig. 4(b)] exhibit only a single peak near 5369 Hz and 5382 Hz, as indicated by the red and yellow curves in Fig. 4(b), which is consistent with the predicted eigenfrequencies of the inner and outer corners. To further demonstrate the non-Hermitian-induced fractal higher-order topological phase, we also plot the site-resolved responses measured at the peak frequencies of the outer corner state, inner corner state, edge state, and bulk state spectra in Figs. 4(c)–(f), respectively. At 5369 Hz, which corresponds to the peak of the outer corner state spectrum, the acoustic intensity measured at the outer corner resonant cavities is much higher than in other regions [Fig. 4(c)], indicating the presence of the outer corner state. In contrast, the responses measured at the peak frequencies of the inner corner state, edge state, and bulk state spectra (5382 Hz, 5412 Hz, and 5425 Hz) are higher in their respective regions [Figs. 4(d)–(f)]. These experimental observations agree well with the numerical simulation results presented in Fig. 3.

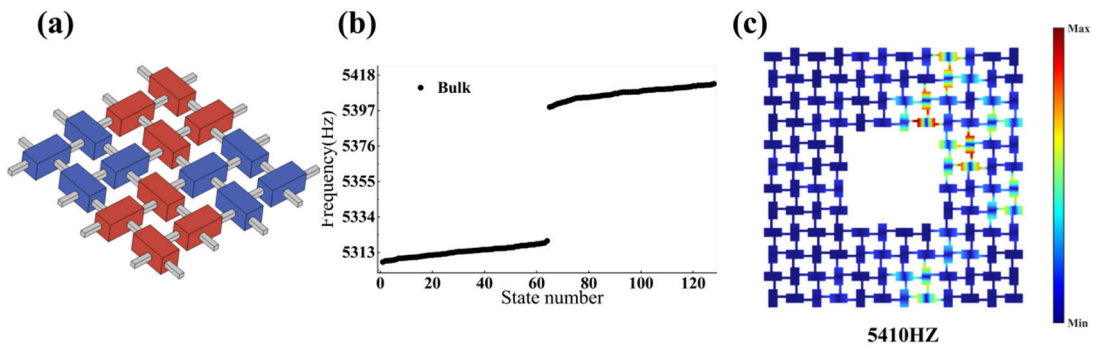


FIG. 5. Numerical simulations of the non-Hermitian acoustic fractal trivial lattice. (a) Schematic of the minimum unit cell of the fractal structure after altering the positions where additional loss is introduced. (b) Energy spectrum of the G(1) fractal lattice obtained through theoretical calculation. It can be observed from the figure that after altering the locations of the introduced loss, the fractal structure transitions from a nontrivial phase to a trivial phase. (c) Bulk state obtained when the ordinate in (b) is set to 5410 Hz.

IV. Flexible tuning of energy concentration of topological states based on the non-Hermitian method

To further verify the effect of loss contrast on the degree of energy concentration in the system, we performed systematic numerical simulations on this non-Hermitian fractal model. As illustrated in Fig. 6(a), the frequency distributions of the edge and corner states, along with the evolution spectra of the energy localization degree as a function of the loss contrast intensity, are calculated and extracted. In these spectra, the localization coefficients of the outer corner, inner corner, and edge states are quantitatively characterized by red, green, and purple color scales, respectively. It can be observed that as the non-Hermitian intensity increases, the characteristic spectral bands representing the outer (red) and inner (green) corner states gradually separate from the edge and bulk states, accompanied by a significant deepening in color saturation. This indicates a pronounced localization enhancement effect within the system at the macroscopic level.

Based on the theoretical calculation results of the extended multiscale finite element method [Fig. 5(b)], the real part of the complex energy spectrum for the trivial group does not exhibit a protected bandgap structure within the corresponding frequency range. Unlike the clear discrete distribution of eigenvalues shown in Fig. 2(b), the energy levels of the trivial group are highly degenerate and lack isolated corner-state or edge-state energy levels. Numerical simulations using the extended multiscale finite element method further reveal this physical discrepancy. The field distribution maps clearly demonstrate that the acoustic energy is not localized at any hierarchical vertices (outer or inner corners) of the fractal structure, but rather is randomly distributed across the lattice in the form of bulk states. This comparison provides compelling evidence that although the fractal geometry itself offers a complex hierarchy of boundaries, the emergence of higher-order topological states strictly relies on the spatial modulation symmetry of the non-Hermitian parameters. By switching the non-Hermitian distribution from a topologically nontrivial configuration to a trivial one, the system transitions from a topological insulator with hierarchical localization characteristics to a conventional trivial phase. This rigorous comparison between theory

and numerical calculations rules out the interference of geometric localization or simple resonance effects, providing solid physical logic support for the "non-Hermitian route induced fractal topology" proposed in this paper.

To further verify the effect of loss contrast on the degree of energy concentration in the system, we performed systematic numerical simulations on this non-Hermitian fractal model. As illustrated in Fig. 6(a), the frequency distributions of the edge and corner states, along with the evolution spectra of the energy localization degree as a function of the loss contrast intensity, are calculated and extracted. In these spectra, the localization coefficients of the outer corner, inner corner, and edge states are quantitatively characterized by red, green, and purple color scales, respectively. It can be observed that as the non-Hermitian intensity increases, the characteristic spectral bands representing the outer (red) and inner (green) corner states gradually separate from the edge and bulk states, accompanied by a significant deepening in color saturation. This indicates a pronounced localization enhancement effect within the system at the macroscopic level.

To deeply investigate the specific acoustic field manifestations of this energy localization effect in physical space, the eigenmode distributions under two distinct parameters, $\Delta\gamma = 5$ and $\Delta\gamma = 12$, are extracted for comparative analysis. Figures 6(b) and 6(c) clearly illustrate the evolution process of the energy localization degree for the outer corner states: when $\Delta\gamma = 5$, although the acoustic field energy of the outer corner state is concentrated at the exterior corners of the structure, a portion of the energy still leaks and diffuses into adjacent lattice sites; whereas when the loss contrast is elevated to $\Delta\gamma = 12$, the acoustic energy is extremely compressed and almost perfectly "pinned" at the outermost single corner site, with the energy leakage into adjacent lattices being significantly suppressed. Similarly, the acoustic field evolution of the inner corner states follows this physical principle. Comparing Fig. 6(d) with Fig. 6(e) reveals that, driven by a relatively high loss contrast $\Delta\gamma = 12$, the energy that originally spread along the inner boundaries to a certain extent is

redistributed and highly precisely localized at specific topological corner sites of the inner defect boundaries.

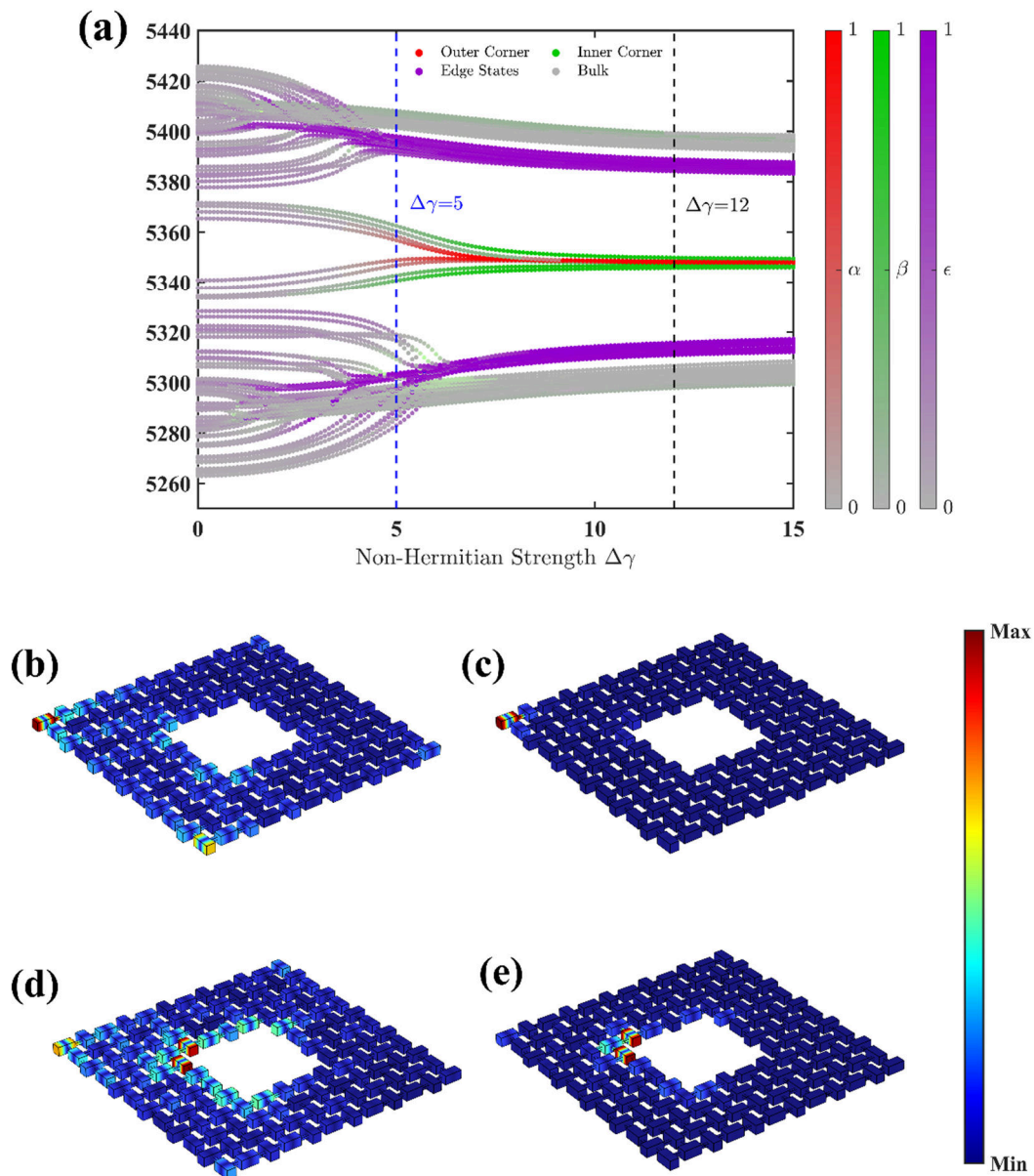


FIG. 6. Numerical simulation results of the effect of loss contrast on the degree of energy concentration within the system. (a) Frequencies and energy concentration degrees of the edge and corner states in the non-Hermitian fractal model as a function of the loss contrast. The red, green, and purple color scales represent the localization coefficient values for the outer corners, inner corners, and edges, respectively. (b), (d) Energy concentration degrees of the outer and inner corner states, respectively, corresponding to a value of $\Delta\gamma = 5$ in (a). (c), (e) Energy concentration degrees of the outer and inner corner states, respectively, corresponding to a value of $\Delta\gamma = 12$ in (a).

V. Conclusion

In this work, through comprehensive and consistent theoretical, numerical, and experimental investigations, we propose and verify a non-Hermitian route to construct higher-order topological insulators in acoustic fractal lattices. This extends the application boundaries of non-Hermitian topological physics into non-integer-dimensional systems and provides a novel paradigm for the multifunctional design of acoustic topological devices. The introduction of additional loss into a fractal system that originally hosted only bulk modes reveals the emergence of inner and outer corner states within the acoustic fractal lattice, thereby subverting the conventional perception of loss as a strictly detrimental factor. Furthermore, numerical simulations demonstrate that altering the loss configuration in the acoustic fractal lattice can also yield a trivial insulator. This conclusively indicates that merely modulating the spatial arrangement of physical loss is sufficient to effectively reshape the topological phases of the fractal acoustic system. Theoretical solutions and numerical evolution results profoundly reveal the central role of loss contrast in determining the degree of acoustic energy localization within the system. Tuning non-Hermitian parameters to control the loss contrast not only provides a nascent mechanism to overcome the limitations of conventional Hermitian physics, but also enables the active and precise manipulation of extreme acoustic localization within complex fractal geometries. This physical capability to achieve highly concentrated acoustic energy on demand holds profound theoretical significance and immense application potential for future practical engineering endeavors, including the development of highly sensitive acoustic detectors, efficient acoustic energy harvesters, and novel topological acoustic components. Additionally, the non-Hermitian-fractal coupled topological mechanism revealed in this study can be directly extended to other classical wave systems, such as photonics and electronics, providing a crucial reference for the cross-disciplinary application of non-Hermitian topological devices.

Appendix A. Site selection for positive and negative couplings

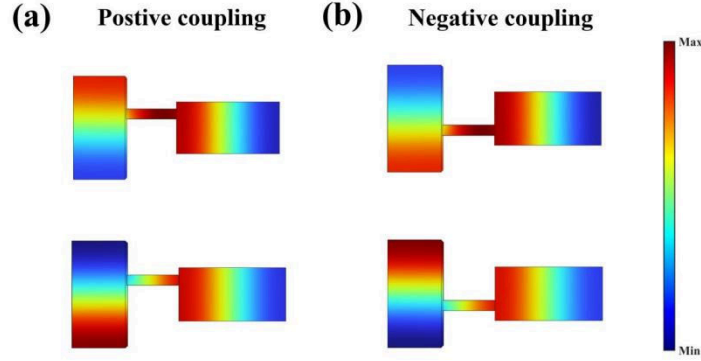


FIG. 7. Eigenmodes of two coupled acoustic resonators. (a) Positive-coupling eigenmodes of two coupled resonators. (b) Negative-coupling eigenmodes of two coupled resonators.

To achieve the π flux required by the BBH model, we realize positive and negative couplings by adjusting the geometric positions of the acoustic coupling tubes. In this paper, positive coupling is defined as the configuration where the connecting waveguide is located at the upper part [Fig. 7(a)], and negative coupling is defined as the configuration where it is located at the lower part [Fig. 7(b)]. In Figs. 7(a) and 7(b), when switching from one configuration to the other, the eigenfrequencies of the two eigenmodes are exchanged, indicating a flip in the coupling sign.

Appendix B. Spectral response of a single resonator and extraction of loss parameters

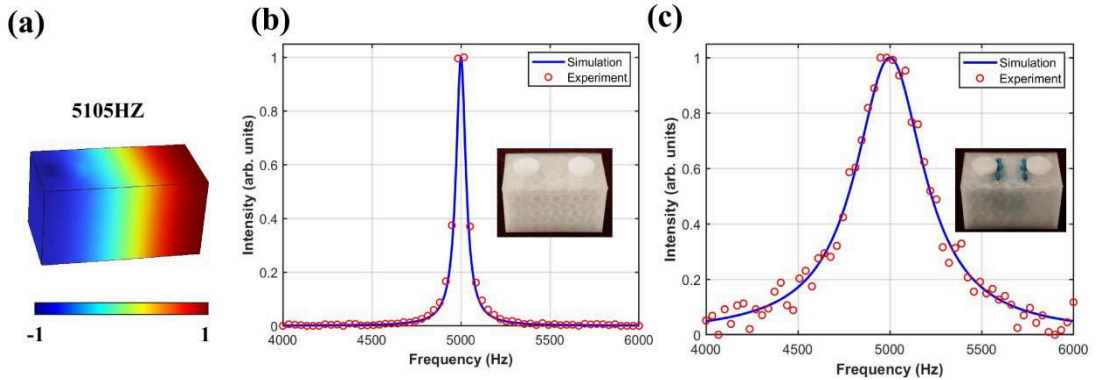


FIG. 8. Measured spectra of a single resonator. (a) Eigenmode of the dipole mode. (b), (c) Measured spectra of a single resonator with additional loss. Red dots represent the measured results, and the blue line indicates the numerical fitting results.

Rectangular acoustic resonant cavities are employed in the experiments. To

accurately extract the simulation parameters, we conducted frequency response tests on a single cavity. As illustrated by the simulated field distribution in Fig. 8(a), the resonance frequency of interest is located around $f \approx 5105$ Hz. This mode exhibits a distinct dipole distribution, which is conducive to forming strong coupling. For a single resonator without additional loss, the measured spectrum exhibits a peak at 5107Hz, as shown in Fig. 8(b). By fitting the experimental spectrum with the blue line, we can account for the background loss in the simulations by setting the speed of sound to $c = 342.34 + 2.23i$ m/s. We also measured the spectrum of the resonator with additional loss, as shown in Fig.8(c). The spectrum broadens, while the peak frequency exhibits almost no shift. Similarly, the speed of sound is estimated to be $c = 342.34 + 14.72i$ m/s. These values are subsequently used in the numerical simulations of the bulk dispersion and eigenmodes for the finite lattices.

Appendix C. Calculation of the Hamiltonian for the fractal non-Hermitian acoustic system

Matrix representation:

$$H_{total} = \bigoplus_{(i,j) \in C_2} H_{intra}^{(i,j)} + \sum_{\substack{(i,j) \sim (i',j') \\ C_2(i,j)=C_2(i',j')=1}} H_{inter}^{(i,j) \leftrightarrow (i',j')}$$

Here, \bigoplus represents the direct sum of the intra-cell Hamiltonians for all nonzero unit cells, and $\sum H$ represents the sum of the inter-cell Hamiltonians between adjacent nonzero unit cells; $(i,j) \sim (i',j')$ indicates that unit cells (i,j) and (i',j') are horizontally or vertically adjacent, and $H_{inter}^{(i,j) \leftrightarrow (i',j')}$ denotes the inter-cell coupling matrix between these two unit cells.

$$H_{AA} = \begin{vmatrix} 0 & \kappa_1 S_1 & 0 & 0 & |\kappa_1| & 0 & 0 \\ & \kappa_1 S_1 & 0 & \kappa_2 S_1 & 0 & |\kappa_1| & 0 \\ 0 & \kappa_2 S_1 & 0 & \kappa_1 S_1 & 0 & 0 & |\kappa_1| \\ 0 & 0 & \kappa_1 S_1 & 0 & 0 & 0 & |\kappa_1| \\ |\kappa_1| & 0 & 0 & 0 & \kappa_1 S_2 & 0 & 0 \\ 0 & |\kappa_1| & 0 & 0 & \kappa_1 S_2 & 0 & \kappa_2 S_2 \\ 0 & 0 & |\kappa_1| & 0 & 0 & \kappa_2 S_2 & 0 \\ 0 & 0 & 0 & |\kappa_1| & 0 & 0 & \kappa_1 S_2 \end{vmatrix}$$

$$H_{AB} = \begin{vmatrix} 0 & 0 & 0 & 0 & 0 & 0 & 0 & 0 \\ 0 & 0 & 0 & 0 & 0 & 0 & 0 & 0 \\ 0 & 0 & 0 & 0 & 0 & 0 & 0 & 0 \\ 0 & 0 & 0 & 0 & 0 & 0 & 0 & 0 \\ |\kappa_1| & 0 & 0 & 0 & 0 & 0 & 0 & 0 \\ 0 & |\kappa_1| & 0 & 0 & 0 & 0 & 0 & 0 \\ 0 & 0 & |\kappa_1| & 0 & 0 & 0 & 0 & 0 \\ 0 & 0 & 0 & |\kappa_1| & 0 & 0 & 0 & 0 \end{vmatrix}$$

$$H_{BA} = \begin{vmatrix} 0 & 0 & 0 & 0 & |\kappa_1| & 0 & 0 & 0 \\ 0 & 0 & 0 & 0 & 0 & |\kappa_1| & 0 & 0 \\ 0 & 0 & 0 & 0 & 0 & 0 & |\kappa_1| & 0 \\ 0 & 0 & 0 & 0 & 0 & 0 & 0 & |\kappa_1| \\ 0 & 0 & 0 & 0 & 0 & 0 & 0 & 0 \\ 0 & 0 & 0 & 0 & 0 & 0 & 0 & 0 \\ 0 & 0 & 0 & 0 & 0 & 0 & 0 & 0 \\ 0 & 0 & 0 & 0 & 0 & 0 & 0 & 0 \end{vmatrix}$$

$$H_{BB} = \begin{vmatrix} 0 & \kappa_1 S_3 & 0 & 0 & |\kappa_1| & 0 & 0 \\ \kappa_1 S_3 & 0 & \kappa_2 S_3 & 0 & 0 & 0 & 0 \\ 0 & \kappa_2 S_3 & 0 & \kappa_1 S_3 & 0 & 0 & |\kappa_1| \\ 0 & 0 & \kappa_1 S_3 & 0 & 0 & 0 & |\kappa_1| \\ |\kappa_1| & 0 & 0 & 0 & \kappa_1 S_4 & 0 & 0 \\ 0 & |\kappa_1| & 0 & 0 & \kappa_1 S_4 & 0 & \kappa_2 S_4 \\ 0 & 0 & |\kappa_1| & 0 & 0 & \kappa_2 S_4 & 0 \\ 0 & 0 & 0 & |\kappa_1| & 0 & \kappa_1 S_4 & 0 \end{vmatrix}$$

$$H_{\text{intra}} = \begin{pmatrix} H_{AA} & H_{AB} \\ H_{BA} & H_{BB} \end{pmatrix}$$

$$H_Z = (0)_{8 \times 8}$$

$$H_{h1} = \begin{vmatrix} 0 & 0 & 0 & 0 & 0 & 0 & 0 & 0 \\ 0 & 0 & 0 & 0 & 0 & 0 & 0 & 0 \\ 0 & 0 & 0 & 0 & 0 & 0 & 0 & 0 \\ 0 & 0 & 0 & 0 & 0 & 0 & 0 & 0 \\ \kappa_2 S_1 & 0 & 0 & 0 & 0 & 0 & 0 & 0 \\ 0 & 0 & 0 & 0 & 0 & 0 & 0 & 0 \\ 0 & 0 & 0 & 0 & 0 & 0 & 0 & 0 \\ \kappa_2 S_2 & 0 & 0 & 0 & 0 & 0 & 0 & 0 \end{vmatrix}$$

$$H_{h2} = \begin{pmatrix} 0 & 0 & 0 & 0 & 0 & 0 & 0 & 0 \\ 0 & 0 & 0 & 0 & 0 & 0 & 0 & 0 \\ 0 & 0 & 0 & 0 & 0 & 0 & 0 & 0 \\ 0 & 0 & 0 & 0 & 0 & 0 & 0 & 0 \\ \kappa_2 S_3 & 0 & 0 & 0 & 0 & 0 & 0 & 0 \\ 0 & 0 & 0 & 0 & 0 & 0 & 0 & 0 \\ 0 & 0 & 0 & 0 & 0 & 0 & 0 & 0 \\ \kappa_2 S_4 & 0 & 0 & 0 & 0 & 0 & 0 & 0 \end{pmatrix}$$

$$H_{\text{inter}}^{\text{horiz}} = \begin{pmatrix} H_{h1} & H_Z \\ H_{h2} & H_Z \end{pmatrix}$$

$$H_{v1} = \begin{pmatrix} 0 & 0 & 0 & 0 & 0 & 0 & 0 & 0 \\ 0 & 0 & 0 & 0 & 0 & 0 & 0 & 0 \\ 0 & 0 & 0 & 0 & 0 & 0 & 0 & 0 \\ 0 & 0 & 0 & 0 & 0 & 0 & 0 & 0 \\ |\kappa_2| & 0 & 0 & 0 & 0 & 0 & 0 & 0 \\ 0 & |\kappa_2| & 0 & 0 & 0 & 0 & 0 & 0 \\ 0 & 0 & |\kappa_2| & 0 & 0 & 0 & 0 & 0 \\ 0 & 0 & 0 & |\kappa_2| & 0 & 0 & 0 & 0 \end{pmatrix}$$

$$H_{\text{inter}}^{\text{vert}} = \begin{pmatrix} H_Z & H_Z \\ H_{v1} & H_Z \end{pmatrix}$$

Eigenvalue equation and energy spectrum calculation:

$$H|\psi_n\rangle = E_n|\psi_n\rangle$$

$E_n = \text{Re}(E_n) + i\text{Im}(E_n)$ is the complex eigenvalue (corresponding to the resonance frequency of the acoustic mode, with the real part representing the frequency value and the imaginary part representing the decay rate), and, $|\psi_n\rangle = \sum_{m=1}^{N_{\text{site}}} \psi_{n,m} |m\rangle$ is the eigenstate (where $\psi_{n,m}$ is the mode amplitude at lattice site m , describing the spatial distribution of the acoustic energy).

Appendix D. Details of the simulation and experimental setup

1. Numerical simulations

All numerical simulations presented in this study were performed using the Pressure Acoustics module in the commercial software COMSOL Multiphysics. In the numerical simulations, the air density of the background medium is set to 1.22kg/m^3 , and the real part of the speed of sound in air is set to 342.34m/s . Loss is introduced by incorporating an imaginary term into the speed of sound. By adjusting the speed of sound to fit the measured and simulated spectra of a single resonator, c is set to $342.34 + 2.23i$ m/s for the resonator considering only background loss, whereas $c = 342.34 + 14.72i$ m/s for the resonator with additional loss. Due to the large acoustic impedance mismatch between the photosensitive resin and air, the boundaries are modeled as sound-hard walls.

2. Experimental setup and measurement methods

2.1. Sample fabrication and experimental measurements

To experimentally verify the non-Hermitian-induced higher-order topological phases in the fractal system, we fabricated the acoustic fractal lattice samples using stereolithography 3D printing technology. The material used is a photosensitive resin (elastic modulus of 2765MPa , density of 1.3g/cm^3) with a printing precision of $\pm 0.1\text{mm}$. The experimental sample comprises 128 acoustic resonators. Small holes with a diameter of 5mm are drilled on both sides of each resonator, which can be opened or closed by two circular cover plates. In addition, 5 small holes with a diameter of 2mm are drilled at both the left and right ends of the resonators corresponding to the blue rectangles in Fig. 4(a). During the experiment, acoustic waves generated by a loudspeaker are introduced into the sample through the small hole on one side of the resonator, and a microphone detects the signal through the small hole on the other side of the same resonator. This measurement is repeated for all resonators in the sample. During the measurements, the perforated cover plates at the excitation and detection sites are opened, while the remaining sites are sealed with cover plates. The blue resonators in the sample maintain an intact structure, whereas the drilled holes on the sidewalls of the red resonators are filled with blue sound-absorbing material (polyurethane foam) to achieve a differential loss configuration [Fig. 4(a)].

2.2. Experimental measurement system

The experimental system consists of a signal generator, a loudspeaker, the 3D-printed acoustic sample, a microphone, a conditioning amplifier, and a data acquisition system [Fig. 9]. The loudspeaker is driven by a signal generator (DG1022U, RIGOL) and a power amplifier (2706, B&K). The signal generator outputs a swept-frequency signal from 5100-5500Hz (with a resolution of 1Hz), which is amplified by the power amplifier to drive the loudspeaker. The acoustic waves are incident through the small hole on one side of the resonator, and the transmitted signals are collected by a microphone (MPA416, BSWA) placed at the small hole on the opposite side. The collected signals are then transmitted to a computer equipped with a control module (MC3242, BSWA) to detect the acoustic response of the waveguides.

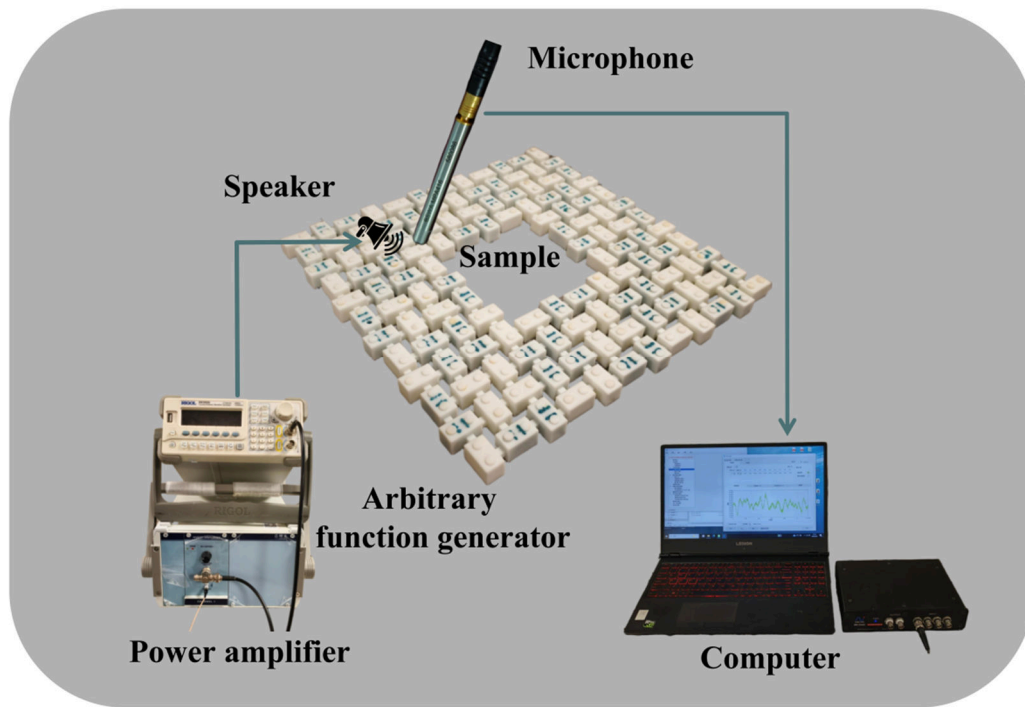


FIG. 9. Experimental setup and procedure.

References:

- [1] T. Ozawa et al., Topological photonics, *Rev. Mod. Phys.* **91**, 015006 (2019).
- [2] M. Z. Hasan and C. L. Kane, *Colloquium* : Topological insulators, *Rev. Mod. Phys.* **82**, 3045 (2010).
- [3] Z. Wang, Y. Chong, J. D. Joannopoulos, and M. Soljačić, Observation of unidirectional

- backscattering-immune topological electromagnetic states, *Nature* **461**, 772 (2009).
- [4] F. D. M. Haldane and S. Raghu, Possible Realization of Directional Optical Waveguides in Photonic Crystals with Broken Time-Reversal Symmetry, *Phys. Rev. Lett.* **100**, 013904 (2008).
- [5] X.-L. Qi and S.-C. Zhang, Topological insulators and superconductors, *Rev. Mod. Phys.* **83**, 1057 (2011).
- [6] L. Lu, J. D. Joannopoulos, and M. Soljačić, Topological photonics, *Nature Photon* **8**, 821 (2014).
- [7] C. He, X. Ni, H. Ge, X.-C. Sun, Y.-B. Chen, M.-H. Lu, X.-P. Liu, and Y.-F. Chen, Acoustic topological insulator and robust one-way sound transport, *Nature Phys* **12**, 1124 (2016).
- [8] Z. Zhang, Y. Tian, Y. Wang, S. Gao, Y. Cheng, X. Liu, and J. Christensen, Directional Acoustic Antennas Based on Valley-Hall Topological Insulators, *Advanced Materials* **30**, 1803229 (2018).
- [9] Y.-G. Peng, C.-Z. Qin, D.-G. Zhao, Y.-X. Shen, X.-Y. Xu, M. Bao, H. Jia, and X.-F. Zhu, Experimental demonstration of anomalous Floquet topological insulator for sound, *Nat Commun* **7**, 13368 (2016).
- [10] R. Fleury, A. B. Khanikaev, and A. Alù, Floquet topological insulators for sound, *Nat Commun* **7**, 11744 (2016).
- [11] B.-Y. Xie, H.-F. Wang, H.-X. Wang, X.-Y. Zhu, J.-H. Jiang, M.-H. Lu, and Y.-F. Chen, Second-order photonic topological insulator with corner states, *Phys. Rev. B* **98**, 205147 (2018).
- [12] Z. Yang, F. Gao, X. Shi, X. Lin, Z. Gao, Y. Chong, and B. Zhang, Topological Acoustics, *Phys. Rev. Lett.* **114**, 114301 (2015).
- [13] G. Ma, M. Xiao, and C. T. Chan, Topological phases in acoustic and mechanical systems, *Nat Rev Phys* **1**, 281 (2019).
- [14] X. Ni, C. He, X.-C. Sun, X. Liu, M.-H. Lu, L. Feng, and Y.-F. Chen, Topologically protected one-way edge mode in networks of acoustic resonators with circulating air flow, *New J. Phys.* **17**, 053016 (2015).
- [15] Z. Song, Z. Fang, and C. Fang, $(d - 2)$ -Dimensional Edge States of Rotation Symmetry Protected Topological States, *Phys. Rev. Lett.* **119**, 246402 (2017).
- [16] W. A. Benalcazar, B. A. Bernevig, and T. L. Hughes, Electric multipole moments, topological multipole moment pumping, and chiral hinge states in crystalline insulators, *Phys. Rev. B* **96**, 245115 (2017).
- [17] F. Schindler, A. M. Cook, M. G. Vergniory, Z. Wang, S. S. P. Parkin, B. A. Bernevig, and T. Neupert, Higher-order topological insulators, *Sci. Adv.* **4**, eaat0346 (2018).
- [18] M. Ezawa, Higher-Order Topological Insulators and Semimetals on the Breathing Kagome and Pyrochlore Lattices, *Phys. Rev. Lett.* **120**, 026801 (2018).
- [19] W. A. Benalcazar, B. A. Bernevig, and T. L. Hughes, Quantized electric multipole insulators, *Science* **357**, 61 (2017).
- [20] J. Langbehn, Y. Peng, L. Trifunovic, F. Von Oppen, and P. W. Brouwer, Reflection-Symmetric Second-Order Topological Insulators and Superconductors, *Phys. Rev. Lett.* **119**, 246401 (2017).
- [21] H. Xue, Y. Yang, F. Gao, Y. Chong, and B. Zhang, Acoustic higher-order topological insulator on a kagome lattice, *Nature Mater* **18**, 108 (2019).
- [22] Y. Qi, C. Qiu, M. Xiao, H. He, M. Ke, and Z. Liu, Acoustic Realization of Quadrupole Topological Insulators, *Phys. Rev. Lett.* **124**, 206601 (2020).
- [23] H. Chen, H. Zhang, Q. Wu, Y. Huang, H. Nguyen, E. Prodan, X. Zhou, and G. Huang, Creating synthetic spaces for higher-order topological sound transport, *Nat Commun* **12**, 5028 (2021).
- [24] C. Lv, R. Zhang, Z. Zhai, and Q. Zhou, Curving the space by non-Hermiticity, *Nat Commun* **13**, 2184 (2022).

- [25] X. Ni, M. Weiner, A. Alù, and A. B. Khanikaev, Observation of higher-order topological acoustic states protected by generalized chiral symmetry, *Nature Mater* **18**, 113 (2019).
- [26] A. Uchiyama, K. Ozeki, Y. Higurashi, M. Kidera, M. Komiyama, and T. Nakagawa, Control system renewal for efficient operation in RIKEN 18 GHz electron cyclotron resonance ion source, *Review of Scientific Instruments* **87**, 02A722 (2016).
- [27] S. A. Cummer, J. Christensen, and A. Alù, Controlling sound with acoustic metamaterials, *Nat Rev Mater* **1**, 16001 (2016).
- [28] B. Verberck and A. Taroni, Nuclear fusion, *Nature Phys* **12**, 383 (2016).
- [29] S. Yao and Z. Wang, Edge States and Topological Invariants of Non-Hermitian Systems, *Phys. Rev. Lett.* **121**, 086803 (2018).
- [30] A. Habib, J. Xu, Y. Ping, and R. Sundararaman, Electric fields and substrates dramatically accelerate spin relaxation in graphene, *Phys. Rev. B* **105**, 115122 (2022).
- [31] M.-A. Miri and A. Alù, Exceptional points in optics and photonics, *Science* **363**, eaar7709 (2019).
- [32] R. El-Ganainy, K. G. Makris, M. Khajavikhan, Z. H. Musslimani, S. Rotter, and D. N. Christodoulides, Non-Hermitian physics and PT symmetry, *Nature Phys* **14**, 11 (2018).
- [33] X. Zhu, H. Ramezani, C. Shi, J. Zhu, and X. Zhang, P T -Symmetric Acoustics, *Phys. Rev. X* **4**, 031042 (2014).
- [34] C. M. Bender and S. Boettcher, Real Spectra in Non-Hermitian Hamiltonians Having P T Symmetry, *Phys. Rev. Lett.* **80**, 5243 (1998).
- [35] K. Kawabata, K. Shiozaki, M. Ueda, and M. Sato, Symmetry and Topology in Non-Hermitian Physics, *Phys. Rev. X* **9**, 041015 (2019).
- [36] Z. Gong, Y. Ashida, K. Kawabata, K. Takasan, S. Higashikawa, and M. Ueda, Topological Phases of Non-Hermitian Systems, *Phys. Rev. X* **8**, 031079 (2018).
- [37] H. Shen, B. Zhen, and L. Fu, Topological Band Theory for Non-Hermitian Hamiltonians, *Phys. Rev. Lett.* **120**, 146402 (2018).
- [38] H. Zhao, X. Qiao, T. Wu, B. Midya, S. Longhi, and L. Feng, Non-Hermitian topological light steering, *Science* **365**, 1163 (2019).
- [39] L. Zhang et al., Acoustic non-Hermitian skin effect from twisted winding topology, *Nat Commun* **12**, 6297 (2021).
- [40] K. J. Falconer, *Fractal Geometry: Mathematical Foundations and Applications*, 2nd ed (Wiley, Chichester, England, 2003).
- [41] T. Biesenthal, L. J. Maczewsky, Z. Yang, M. Kremer, M. Segev, A. Szameit, and M. Heinrich, Fractal photonic topological insulators, *Science* **376**, 1114 (2022).
- [42] B. B. Mandelbrot, *The Fractal Geometry of Nature* (W.H. Freeman, San Francisco, 1982).
- [43] H. Fan, H. Gao, T. Liu, S. An, Y. Zhu, H. Zhang, J. Zhu, and Z. Su, Acoustic non-Hermitian higher-order topological bound states in the continuum, *Applied Physics Letters* **126**, 071702 (2025).
- [44] Q. Zhang, Y. Leng, L. Xiong, Y. Li, K. Zhang, L. Qi, and C. Qiu, Construction and Observation of Flexibly Controllable High-Dimensional Non-Hermitian Skin Effects, *Advanced Materials* **36**, 2403108 (2024).
- [45] H. Gao, W. Zhu, H. Xue, G. Ma, and Z. Su, Controlling acoustic non-Hermitian skin effect via synthetic magnetic fields, *Applied Physics Reviews* **11**, 031410 (2024).
- [46] H. Gao, W. Zhu, H. Xue, G. Ma, and Z. Su, Controlling acoustic non-Hermitian skin effect via synthetic magnetic fields, *Applied Physics Reviews* **11**, 031410 (2024).

- [47] Z. Gu, H. Gao, P.-C. Cao, T. Liu, X.-F. Zhu, and J. Zhu, Controlling Sound in Non-Hermitian Acoustic Systems, *Phys. Rev. Applied* **16**, 057001 (2021).
- [48] Z.-H. Li, L.-X. Xie, X. Gao, W. Huang, Y. Xu, J. Yang, M.-H. Lu, and X. Zhong, Koch snowflake-inspired acoustic metasurface for broadband sound diffusion in automotive loudspeaker systems, *Journal of Applied Physics* **138**, 183102 (2025).
- [49] V. Achilleos, G. Theocharis, O. Richoux, and V. Pagneux, Non-Hermitian acoustic metamaterials: Role of exceptional points in sound absorption, *Phys. Rev. B* **95**, 144303 (2017).
- [50] X. Xie, F. Ma, W. B. Rui, Z. Dong, Y. Du, W. Xie, Y. X. Zhao, H. Chen, F. Gao, and H. Xue, Non-Hermitian Dirac cones with valley-dependent lifetimes, *Nat Commun* **16**, 1627 (2025).
- [51] T. Liu, Y. Li, Q. Zhang, and C. Qiu, Observation of Z_2 Non-Hermitian Skin Effect in Projective Mirror-Symmetric Acoustic Metamaterials, *Advanced Materials* **37**, 2506739 (2025).
- [52] E. Zhao, Z. Wang, C. He, T. F. J. Poon, K. K. Pak, Y.-J. Liu, P. Ren, X.-J. Liu, and G.-B. Jo, Two-dimensional non-Hermitian skin effect in an ultracold Fermi gas, *Nature* **637**, 565 (2025).
- [53] Z.-H. Li, L.-X. Xie, X. Gao, W. Huang, Y. Xu, J. Yang, M.-H. Lu, and X. Zhong, Koch snowflake-inspired acoustic metasurface for broadband sound diffusion in automotive loudspeaker systems, *Journal of Applied Physics* **138**, 183102 (2025).